Applied Catalysis B: Environmental 98 (2010) 138–146

Contents lists available at ScienceDirect

Applied Catalysis B: Environmental

journal homepage: www.elsevier.com/locate/apcatb

Controllable synthesis of Bi_2MoO_6 and effect of morphology and variation in local structure on photocatalytic activities

Liwu Zhang[a], Tongguang Xu[a], Xu Zhao[b], Yongfa Zhu[a,*]

[a] Department of Chemistry, Tsinghua University, Beijing 100084, PR China
[b] State Key Laboratory of Environmental Aquatic Chemistry, Research For Eco-Environmental Science, Chinese Academy of Sciences, Beijing 100085, PR China

ARTICLE INFO

Article history:
Received 6 December 2009
Received in revised form 9 May 2010
Accepted 23 May 2010
Available online 1 June 2010

Keywords:
Photocatalysis
Visible-light
Bi_2MoO_6
Local structure
Nanosheet

ABSTRACT

Highly crystalline orthorhombic Bi_2MoO_6 particles with high visible-light photocatalytic activity have been controllably synthesized via a facile hydrothermal process without adding any surfactant. The morphologies of Bi_2MoO_6 with nanosheet and microrod can be selectively obtained by adjusting the pH value of the reactant. The formation mechanisms of nanosheet and microrod structures were then discussed based on the H^+ cations adsorption abilities on different crystal faces. The Bi_2MoO_6 samples prepared at acidic condition showed 12 times higher photocatalytic activity than that prepared at basic condition under visible-light irradiation. The reason for the big difference in the photocatalytic activities for the Bi_2MoO_6 samples obtained at different pH values were systematically studied based on their shape, size and the variation of local structure.

© 2010 Elsevier B.V. All rights reserved.

1. Introduction

The photodecomposition of organic compounds and water splitting by semiconductor photocatalysts has attracted intense research interest because of their economic and ecologically safe option for solving energy and pollution problems [1]. In the past several decades, the thoroughly studied conventional TiO_2 displays excellent activities and stabilities. However, the deficiency of requiring UV light for effective photocatalysis severely hinders the overall process to be used in practical. Therefore, the development of a visible-light photocatalyst consequently has become an imperative topic in current photocatalysis research. Considering the relatively slow reaction rate and poor solar efficiency of TiO_2 which hindered its application, many studies have been carried out to exploit new visible light-driven photocatalysts.

As a typical Aurivillius oxide, Bi_2MO_6 (M = W, Mo) with the layered bismuth oxide family are of special interest due to their dielectric, ion-conductive, luminescent and catalytic properties [2–4]. Recent results revealed that Bi_2MO_6 could perform as an excellent photocatalyst and solar-energy-conversion material for water splitting and degradation of organic compounds under visible-light irradiation [5–10]. The properties of materials with the same composition but different morphologies could be substantially different. Therefore, the better performance of material is not only depended on the compositions but also on the morphologies of the materials. The dependence of the properties of nanomaterials on both the size and shape is a phenomenon of both fundamental scientific interest and many practical and technological applications [11–13]. In order to advance the basic understanding of the principles that determine the shape and to provide tailored building blocks for nanodevices, a variety of methods have been developed to control the shape, dimensionality, and assembly of nanostructures [14,15]. As known, both the size and the morphology have an influence on the properties of semiconductor oxides. For example, nanoscale photocatalysts are believed to perform better than the bulk materials due to the higher surface-to-volume ratio and separation efficiency of the photogenerated electrons or holes [16,17]. The photocatalytic activities of Bi_2WO_6 and $BiVO_4$ nano and microstructures are strongly determined by the shape, size, and structure. Morphology control provides a greater versatility for tuning the photocatalytic properties of semiconductor materials. However, seldom successes in developing approaches to tune the shape and structure of the visible-light-driven photocatalysts have been achieved. As far as we know, the systematic research on the morphology evolutions of Bi_2MoO_6 in different dimensions is rarely concerned. Constructing novel nanostructures by bottom-up techniques may be rationally designed.

In this work, Bi_2MoO_6 nanocrystals were controllably synthesized with tunable morphology by a simple hydrothermal method. The as-prepared Bi_2MoO_6 nanocrystals showed high photocatalytic activity in the decomposition of Methylene blue (MB) under visible-light irradiation. The influence of reaction parameter (pH value) on

* Corresponding author. Tel.: +86 10 62787601; fax: +86 10 62787601.
E-mail address: zhuyf@mail.tsinghua.edu.cn (Y. Zhu).

0926-3373/$ – see front matter © 2010 Elsevier B.V. All rights reserved.
doi:10.1016/j.apcatb.2010.05.022

the Bi_2MoO_6 morphology, structure and the relationship between the morphology and photocatalytic activities were investigated. The aim of this research was to develop a method for the fabrication of different-dimensional Bi_2MoO_6 nanomaterials enriching the available methods for preparation of multicomponent metal oxide, and to adjust the properties by modulating the morphology and size of the materials, thus facilitating their applications.

2. Experimental

2.1. Preparation

All chemicals were analytically pure and used without further purification. For the synthesis of Bi_2MoO_6, 2 mmol $Bi(NO_3)_3{\cdot}5H_2O$ (0.97 g) was dissolved in 20 mL nitric acid solution (2 mol L^{-1}) and stirred for several minutes. Then 0.1 mol L^{-1} Na_2MoO_4 solution (10 mL) was slowly added into the above solution. The amorphous white precipitate formed immediately. The different pH values of the solution (1, 3, 5, 7, 9, 11, 13) were then adjusted with concentrated ammonia under stirring. After being vigorously stirred for 30 min, the resulting precursor suspension was transferred into a 40 mL capacity Teflon-lined stainless steel autoclave, which was subsequently heated to 180 °C and maintained for 24 h. Subsequently, the autoclave was cooled to room temperature naturally. The obtained samples were filtered, washed with deionized water and dried at 80 °C in air.

2.2. Characterization

X-ray powder diffraction (XRD) patterns were obtained on a Bruker D8 Advance X-ray diffractometer at 40 kV and 40 mA with Cu Kα radiation. The crystallite size was calculated from X-ray line broadening via the Scherrer equation: $D = 0.89\lambda/\beta\cos\theta$, where D is the crystal size in nm, λ the Cu $K_{\alpha1}$ wavelength (1.5406 Å), β is the half-width of the peak in radians, and θ is the corresponding diffraction angle. Scanning electron microscopy (SEM) was operated on a JEOL JSM-6700F field-emission scanning electron microscope. Transmission electron microscopy (TEM) was performed using a JEOL JEM 2010 EX instrument at an accelerating voltage of 200 kV. The powder particles were supported on a carbon film coated on a 3 mm diameter fine-mesh copper grid. A suspension in ethanol was sonicated, and a drop was dripped on to the support film. The UV–vis diffuse reflectance spectra (UV–vis DRS) of the samples were obtained on a UV–vis spectrophotometer (UV-3010, Shimadzu) using an integrating-sphere accessory. $BaSO_4$ was used as a reflectance standard. Nitrogen adsorption–desorption measurements were conducted at 77.35 K on a Micromeritics Tristar 3000 analyzer. The Brunauer–Emmett–Teller (BET) surface area was measured with ASAP 2020M (Micromeritics Instrument Corp.). Raman spectra were recorded on a microscopic Raman spectrometer (Renishaw 2000 NR) with an excitation of 514.5 nm laser light.5 mW of the laser power was focused (spot size 5 mm) at the sample. The scattered light was collected in the 180° backscattering geometry. With this setup it is possible to monitor the Raman spectra with a spatial resolution of 5 mm. Spectra were collected in the range of 100–1000 cm^{-1} with a resolution of 1 cm^{-1}. Infrared transmission spectra were recorded for KBr disks containing the powder sample with a FTIR spectrometer (PerkinElmer 1600).

2.3. Photocatalytic activity measurements

The photocatalytic activities of Bi_2MoO_6 samples were evaluated by the degradation of MB in an aqueous solution. A 500 W Xe lamp with a cutoff filter (λ > 420 nm) was used as light resource to ensure the photoreaction proceeded under visible-light irradiation. The reaction cell was placed in a sealed black box of which the top was open and the cutoff filter was set on the window face of the reaction cell to ensure the desired irradiation condition. In each experiment, photocatalyst powders (0.10 g) were added into MB solution (10^{-5} mol L^{-1}, 100 mL). Before illumination, the suspensions were magnetically stirred in the dark for 60 min to reach the adsorption–desorption equilibrium between the photocatalysts and MB. At given time intervals, 3 mL of the aliquots were sampled and centrifuged to remove photocatalyst powders. The degraded solution was analyzed using UV–vis spectrophotometer and absorption peak at 663 nm was monitored.

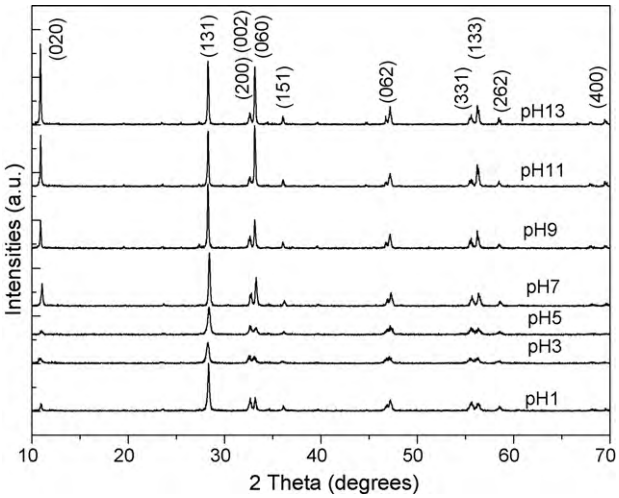

Fig. 1. XRD patterns of samples obtained at different pH values after 24 h at 180 °C. (A) pH 1, (B) pH 3, (C) pH 5, and (D) pH 7, (E) pH 9, (F) pH 11, and (G) pH 13.

3. Results and discussions

3.1. Structure, morphology and formation mechanism

The effects of pH values on the structure and morphology of Bi_2MoO_6 prepared without any surfactant were studied. The precursor suspensions were adjusted to the desired pH values by adding $NH_3{\cdot}OH$ solution, and then were hydrothermally treated at 180 °C for 24 h. The Bi_2MoO_6 samples prepared from the precursor suspensions with pH values of 1, 3, 5, 7,9,11, and 13 are denoted as pH 1, pH 3, pH 5, pH 7, pH 9, pH 11, and pH 13, respectively.

Fig. 1 shows the XRD patterns of Bi_2MoO_6 samples prepared by hydrothermal procedure at different pH values (A–G: pH 1–13). The diffraction peaks of all the samples can be indexed as a pure koechilinite phase, which are consistent with the literature values (JCPDS 76-2388). As can be seen from the XRD patterns, the high crystallinity can be obtained at a relatively low hydrothermal treatment temperature (180 °C). When the pH value is maintained at pH 1, pH 3, pH 5, the expanded diffraction peaks obviously reveal that the crystalline phase would be nanosized. The influence of pH value on the crystalline phase was demonstrated through the changes of XRD patterns. As the pH value increases from 1 to 13, the shape of diffraction peaks become more clean-cut and the intensities increases gradually, indicating better crystallines formed. The crystallines grow larger as estimated according to the width of peak on the basis of the Scherrer equation. It is noteworthy that the XRD patterns also indicate that there are large differences in the relative intensities based on the (0 2 0), (1 3 1), (2 0 0), (0 0 2) and (0 6 0) peaks for all the samples, indicating the possibility of different preferential orientation growth under different pH conditions. For the samples prepared at acid conditions (pH 1, pH 3 and pH 5), the ratio of intensity of (1 3 1)/(2 0 0) is about three, while the standard intensity of the (1 3 1) peak of the XRD pattern is about five times

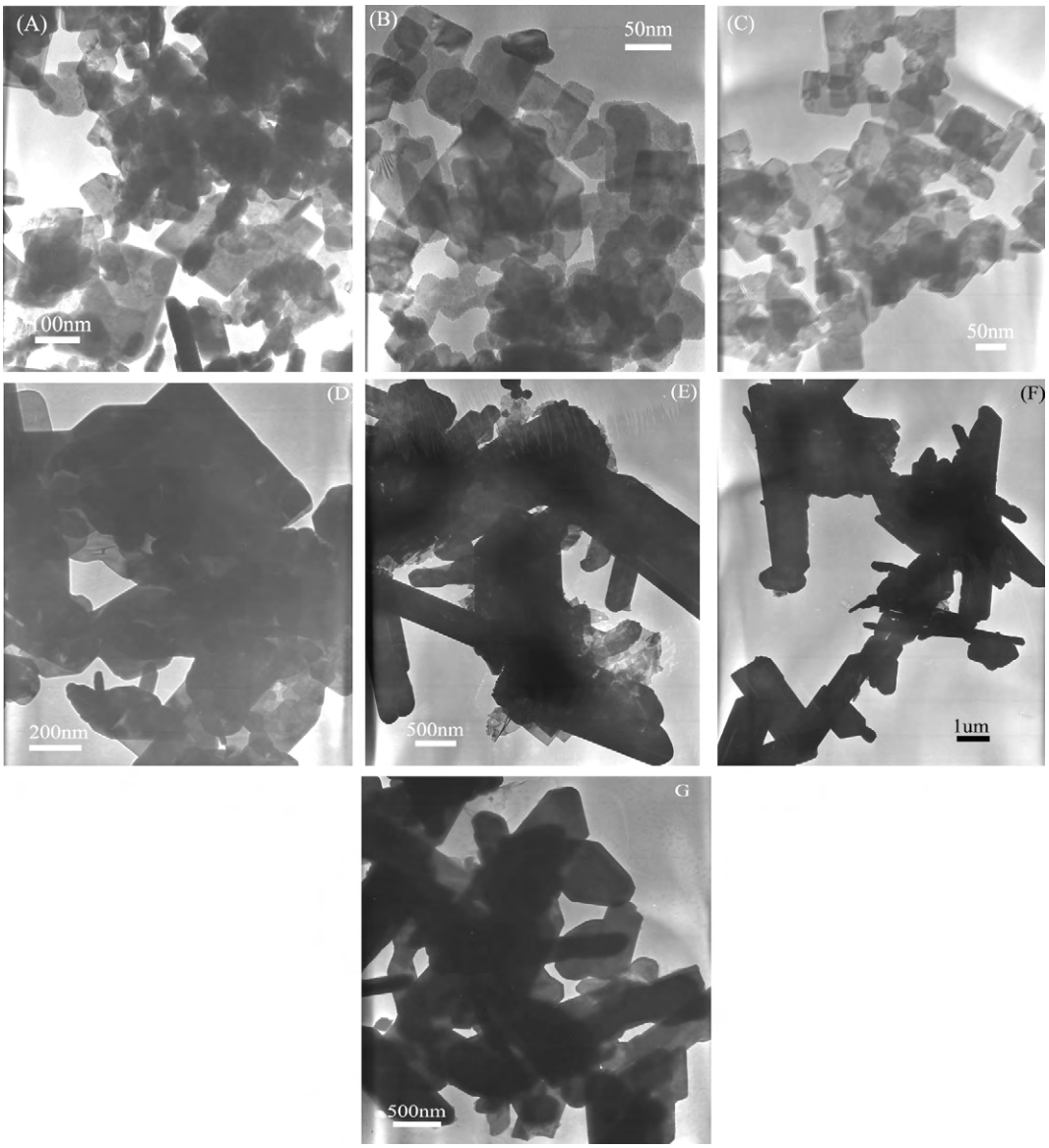

Fig. 2. TEM images of Bi_2MoO_6 samples prepared at different pH values: (A–G) pH 1–13 (hydrothermally treated at 180 °C for 24 h, no surfactant).

stronger than that of the (2 0 0) peak. This implies that the crystal has special anisotropic growth. These results can be attributed to the square-plate structure of the crystallites, which is proved by further study of morphologies of the crystallites. However, the changes of diffraction peaks for the samples (D–G) obtained at base conditions are different with the samples at acid conditions (A–C). As is shown in Fig. 1, the intensities of (1 3 1) peak are similar for all the four samples (D–G), while the intensities of (0 2 0) and (0 6 0) peaks increased greatly, indicating that there must be a different preferential growth orientation in Bi_2MoO_6 under basic conditions. The crystal would grow along the (0 1 0) direction and form 1D rod-like materials.

As a further confirmation of the XRD analysis, Fig. 2 shows the morphological evolution of Bi_2MoO_6 samples with different pH values of the precursor suspensions (A–G: pH 1, pH 3, pH 5, pH 7, pH 9, pH 11, pH 13). When the pH values in the reaction system are kept at 1, 3 and 5, sheet-like Bi_2MoO_6 crystals with the thickness of several nanometers are observed. Interestingly, under acidic condition, the size of the as-obtained Bi_2MoO_6 nanosheets grows smaller with the increasing of the pH values of the reaction system. The width of the nanosheets is about 150, 80 and 50 nm for samples (A–C), respectively. Further increasing the pH value leading to the shape of the as-obtained nanostructures evolved from nanosheets to nanoplates with the thickness of tens of nanometers (D: pH 7). The pH-dependent experiments are taken subsequently by increasing the pH values to 9, 11 and 13. Fig. 2 indicates that the as-prepared Bi_2MoO_6 almost exhibits a rod shape with an average diameter of about 1 μm and length of about 3 μm, which is very different from the morphologies of samples obtained under acid conditions. The above results suggest that the morphology of Bi_2MoO_6 nanosheets/microrods strongly depends on the initial pH of the dispersion. Similar results were also observed in the synthesis of some tungstates [18]. Therefore, the morphology of the as-prepared molybdate nanosheets/microrods can be controlled by tuning the pH value of colloidal precursor.

Fig. 3 shows the HRTEM images of Bi_2MoO_6 samples prepared at different pH values (Fig. 3A–C) and SEM image of Bi_2MoO_6 sample prepared at pH 7 (Fig. 3D). The nanoplate structure is clearly observed from Fig. 3D, which is in accordance with the TEM results. HRTEM images indicate the single-crystalline nature of the samples. For the sample prepared at pH $\leq$7, the d spacing of 0.305 nm corresponding to the lattice spacing of (1 3 1) of orthorhombic

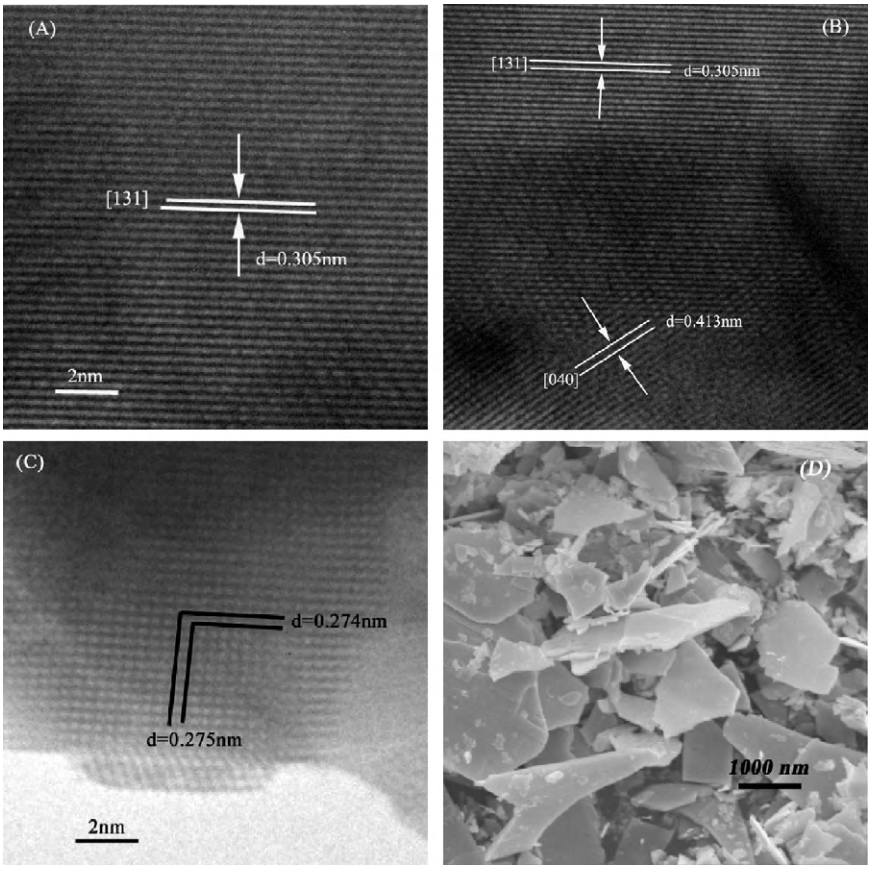

Fig. 3. HRTEM images of Bi_2MoO_6 samples prepared at different pH values: (A) pH 3, (B) pH 7, and (C) pH 11. (D) SEM image of the Bi_2MoO_6 sample prepared at pH 7 (hydrothermally treated at 180 °C for 24 h, no surfactant).

Bi_2MoO_6 is observed from Fig. 3A and B. For the sample prepared at basic condition (pH 11), it can be measured that the d spacings are 0.274 and 0.275 nm, which agree well with the lattice spacings of (0 0 2) and (2 0 0), respectively.

One of the critical factors responsible for the shape determination of the nano- and microcrystals is the crystallographic phase of the initial seed. Once the crystalline phase is determined, the characteristic cell structures of the seeds strongly affect the further crystal growth [19]. As is known, the structure of koechlinite Bi_2MoO_6 consists of alternating $(Bi_2O_2)_n^{2+}$ layers and perovskite-like $(MoO_4)_n^{2-}$ layers, and octahedral Mo chains usually play an important role in the high intrinsic anisotropic growth in various molybdates [20].

In our experiments, it was noted that there was no phase transformation process for all the samples accompanied with morphology variation during the crystal growth. However, the pH value of the growth solution was a crucial parameter in the control of morphology of Bi_2MoO_6 nano- and micro-crystals. The main effect of tuning the pH value was to modulate the kinetics of nucleation and growth of the crystal by controlling experimentally the surface free energy. The preferential adsorption of molecules and ions in solution onto different crystal facets directed the growth of particles into various shapes by controlling the growth rates along different crystal axes [21–24]. The crystal plane with a higher surface energy is expected to have a faster growth rate. Herein, the differences in the pH values showed a significant effect on the selective adsorption of H^+ onto the different surfaces of growing Bi_2MoO_6 crystallites, giving rise to the difference of the growth rates between the different crystallographic directions. At pH 1, pH 3, pH 5 there would be abundant H^+ in the system to adsorb on the (0 1 0) faces and even on (0 0 1) and (1 0 0) faces. Therefore, the surface energy of these faces would all be markedly reduced. Thus, it is possible to form a relatively thin nature along [0 1 0] direction [25]. It is well known that under the hydrothermal environment, nuclei could grow freely in aqueous solution (an open space) to form the nanocrystals with their natural habit, i.e., nanorods, nanoflowers, nanocubes, etc. Further crystal growth for the formation of 2D nanostructures was strongly related to the intrinsic crystal structure of Bi_2MoO_6. It has been reported that orthorhombic Bi_2MoO_6 is constructed by a cornershared MoO_6 octahedral layer and $[Bi_2O_2]^{2+}$ atom layers sandwiched between MoO_6 octahedral layers. It is well known that the shape of the nanostructures is strongly dependent on the relative chemical potential. It is believed that two-dimensional growth occurs only if the chemical potential of two surfaces is much higher than others. On the basis of Bi_2MoO_6 structure, the chains of octahedral-Mo equally exist along the *a* and *c* axes. The facets which are perpendicular to these chains usually have a much higher chemical potential in comparison with other facets. The above feature resulted in faster growth rates of these faces, and thus the crystal growth was preferentially along the layer. Because the Bi_2MoO_6 have an orthrohombic crystal structure, crystal symmetries along *a*, *c* axes should be equivalent. Therefore, the direction of the nanosheets stacking is along the *b* axis, perpendicular to *a* and *c* axes of the planes, and each layer has the same *a* and *c* axes. Based on the experimental results, it can be concluded that under a low pH value condition, there existed higher surface energy on the (1 0 0) and (0 0 1) planes compared with other crystal planes, and the growth of nanocrystal along the (0 1 0) plane was inhibited. The surface cleavage of Bi_2MoO_6 crystal also provides further information for explaining the adsorption of H^+ cations (Fig. 4). As seen from the figure, the (1 0 0), (0 1 0) and (0 0 1) crystal planes are terminated with Mo, O and Bi atoms, respectively. The zigzag

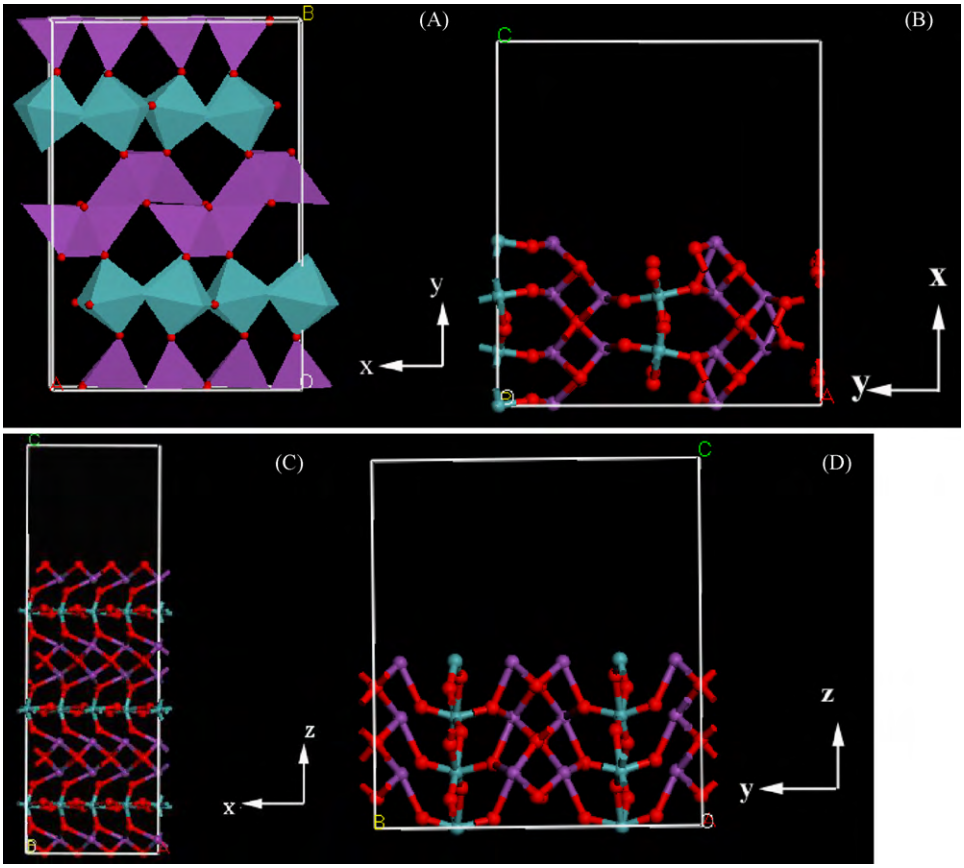

Fig. 4. The structure model illustration of Bi_2MoO_6 crystals (2 × 2 lattices): (A) *xy* projection; the surface structure cleavage of Bi_2MoO_6 crystals: (B) (1 0 0); (C) (0 1 0); (D) (0 0 1). The red, purple and blue balls are denoted as O, Bi and Mo, respectively. (For interpretation of the references to colour in this figure legend, the reader is referred to the web version of the article.)

orientations of Mo octahedral anions on (1 0 0) face results in this face becoming unfavorable for the adsorption of H^+ cations. The amount of O atoms on the (0 1 0) plane is much higher than other planes (Fig. 4C). Therefore, H^+ cations would prefer to absorb on the (0 1 0) planes because of the high density of oxygen atoms on this face, resulting in the crystal growth rate along the (0 1 0) orientation is slowed and formed nanosheets.

However, when $NH_3{\cdot}H_2O$ (1 M) was added to the growth suspension, the H^+ ions were partially neutralized, which makes the localized concentration of H^+ varied on the nanocrystal surface and results in the surface free energies of the various crystallographic planes differing significantly. Obviously, the growth rate of those facets possessing higher free energy would be relatively faster, which affords the possibility of breaking the natural growth habit of the crystal and creating additional growth anisotropy. As revealed in the experiments, Bi_2MoO_6 microrods can be obtained by tuning the pH of the growth solution [26]. Under the alkaline condition (pH 9, pH 11, pH 13), the dominant adsorption of OH^- onto the facets lowers the surface energy of these facets, subsequently prohibits the enlargement in *a*, *b* planes and drives the growth of nuclei along the directions of [0 1 0] [27]. This is coincident with the XRD results. In the XRD pattern of the corresponding samples (Fig. 1F–H), the strongest reflection is (0 2 0), which is quite different from the literature data. This abnormal intensity of the (0 1 0) peak suggests the preferential orientation growth along the [0 1 0] direction to a great degree.

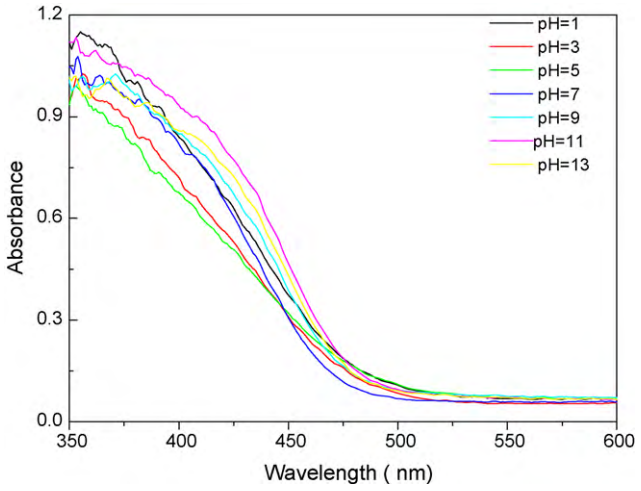

Fig. 5. UV–vis diffuse reflectance spectra of Bi_2MoO_6 powders (A–G: pH 1, pH 3, pH 5, pH 7, pH 9, pH 11, pH 13).

3.2. Optical properties and photocatalytic performances

Optical absorption of Bi_2MoO_6 samples was measured by UV–vis spectroscopy. Fig. 5 exhibits the diffuse reflectance spectra of the Bi_2MoO_6 samples (A–G: pH 1–13). As can be seen, all the Bi_2MoO_6 samples showed strong photoabsorption properties from the UV light region to the visible-light region with the wavelength shorter than 490 nm. The steep shape of the spectra indicated that the visible-light absorption is arisen from the band-gap transition but not from the impurity level [28]. In this system, slight red shift of the absorption band edge of Bi_2MoO_6 samples (from 2.81 to 2.85 eV) can be observed with the pH value increasing from 1

Table 1
Size, BET surface areas and adsorption percentages of photocatalysts in the dark.

Sample	pH 1	pH 3	pH 5	pH 7	pH 9	pH 11	pH 13
Average size (μm)	~0.1	~0.07	~0.05	~0.4	~1	~3	~2
BET surface areas ($m^2\ g^{-1}$)	6.48	17.32	18.75	6.03	5.78	4.41	0.79
Adsorption (%) in dark	45	74	76	32	27	18	9

to 13. It is well known that the band gap energy of semiconductor nanoparticles increases with the decrease of grain size. Herein, Bi_2MoO_6 with a 1D microstructure (pH 9, pH 11, pH 13) had a red shift in the band-gap transition compared with sheet-like Bi_2MoO_6 (pH 1, pH 3, pH 5, pH 7), attributed to the smaller grain sizes of the building blocks of the 2D nanostructures than that of the 1D microrods.

Methylene blue was used as a probe in the heterogeneous photocatalysis, the dark adsorption (on the surface of semiconductor oxide), subsequent decoloration and decomposition can be monitored via visible-light absorption signature (at λ_{max} = 664 nm). Fig. 6 shows the dependence of visible-light photocatalytic activity of the Bi_2MoO_6 samples upon pH values (A–G: pH 1–13) of the precursor suspensions. The blank test demonstrates that the degradation of MB is extremely slow without a photocatalyst under visible-light illumination. The first-order linear relationship was revealed by the plots of $\ln(C/C_0)$ versus irradiation time (t). It was found that the obtained Bi_2MoO_6 samples under acid conditions exhibited much higher photocatalytic activity than other samples. More than 90% of MB could be decomposed with the Bi_2MoO_6 samples prepared at acid condition under visible-light irradiation within 120 min, while only 9% of MB was photodegraded with the sample prepared at basic condition. The calculated apparent reaction rate constant k for the sample prepared at pH 5 was 0.016 min^{-1}, which is more than 12 times faster than that of Bi_2MoO_6 prepared at pH 11 (k = 0.0013 min^{-1}). The vastly different photodegradation rates of MB by different Bi_2MoO_6 samples (A–G) indicated that the photocatalytic performances of these Bi_2MoO_6 samples are greatly different and are strongly dependent on shape, crystal size, and structure.

The lower pH values of the precursor suspensions the higher the photocatalytic activities of the Bi_2MoO_6 samples exhibited. Table 1 shows the average size, Brunauer–Emmett–Teller (BET) surface areas and the adsorption percentages of MB on the photocatalysts in the dark for 60 min. It is clearly revealed that the samples with small size (pH 3, pH 5) can more efficiently absorb the MB due to their higher BET surface area than other samples with larger sizes. The decrease of grain radius reduces the opportunities for recombination and promotes the transfer of the light-generated charge to the surface to degrade the absorbed MB molecules [29]. In addition, with the transformation of Bi_2MoO_6 from a 2D plate-like structure to a 1D rod-like microstructure (samples prepared at pH 1–13), the BET surface area of the samples decreases, resulting in an decrease of adsorption percentages of MB molecules. The increasing of BET surface areas and the decrease of crystalline grains were both beneficial to the enhancement of the photocatalytic activity of Bi_2MoO_6 [30].

Visible-light irradiation of aqueous MB/Bi_2MoO_6 dispersions leads to a decrease in absorption intensity and a blue-shift of the wavelength as the MB degrades. UV–vis spectra taken over time during the photodegradation of MB mediated by Bi_2MoO_6 nanosheets versus microrods are shown in Fig. 6B and C, respectively. A control experiment on an aqueous MB solution in the absence of Bi_2MoO_6 photocatalyst was carried out under the same experimental conditions, but the absorption intensity and absorption wavelength hardly changed with increasing irradiation time. From Fig. 6A it can be concluded that the degradation rate of MB mediated by nanosheets is much faster than that mediated by

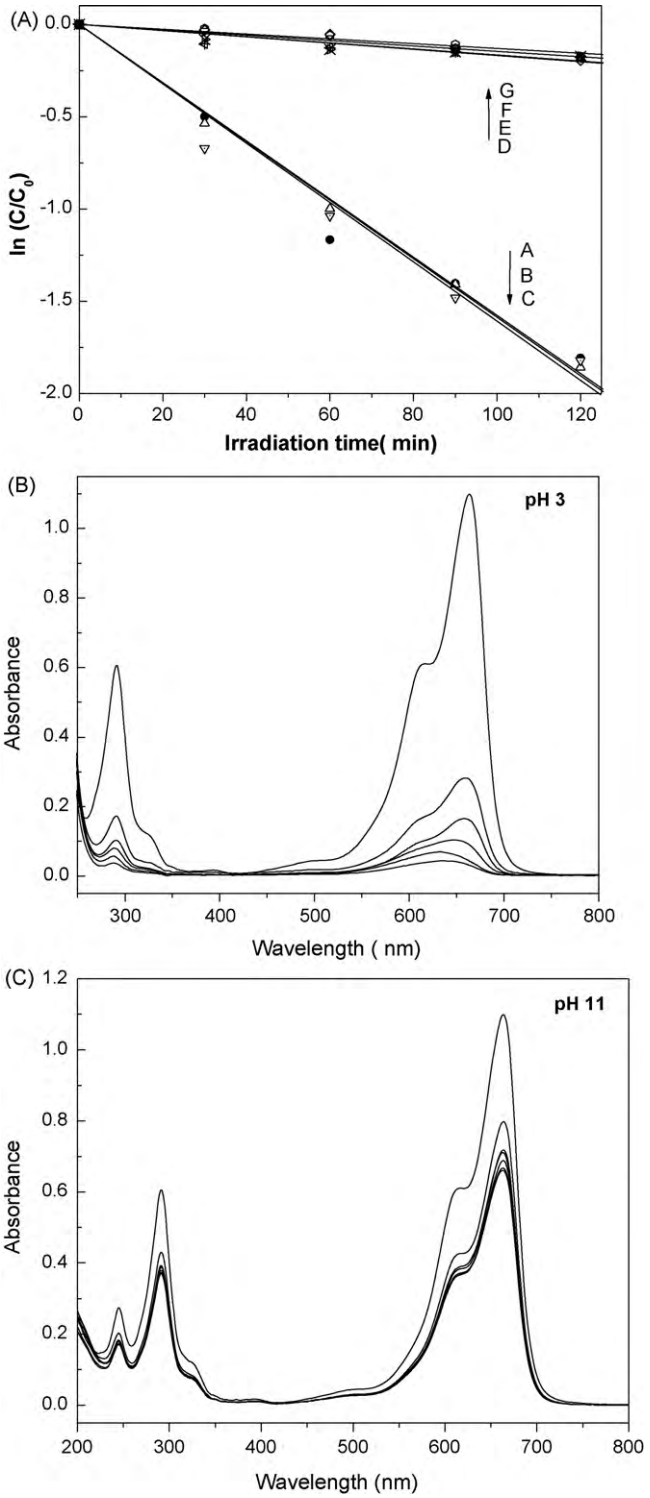

Fig. 6. Photocatalytic degradation of MB in the presence of as-prepared photocatalysts (A–G: pH 1, pH 3; pH 5, pH 7, pH 9, pH 11 and pH 13).

the microrods. The blue-shift of the absorption band from 664 to 610 nm arises from the degradation of MB [31]. After irradiation for 120 min the absorption blue-shifts from 664 to 629 nm in the presence of the prepared nanosheets, indicating that MB has accomplished a demethylation step, while in the same time period it only blue-shifted from 664 to 661 nm using microrods as catalyst. The results confirm that the Bi_2MoO_6 nanosheets had superior photocatalytic activities compared with the microrods. This high photocatalytic activity must be related to the higher surface area of the nanosheets. Moreover, The thickness of the nanosheets results in a relatively large distortion of the unit cell due to the large surface strain, and the nanosheet structure means that electron–holes generated inside the crystal easily transfer to the surface and react with MB [30]. Thus, a higher photocatalytic activity was exhibited compared to the microrods. In addition, XRD and TEM techniques are applied to evaluate the stability of Bi_2MoO_6 after photocatalytic reaction cycles. Results showed that the photocatalytic activity of the pH 5 sample remains almost the same in several consecutive runs for the photodegradation of MB under visible-light illumination ($\lambda > 420$ nm).

The photocatalytic property of Bi_2MoO_6 is also related to the distortion of the M-O polyhedron in crystal structure. Raman spectroscopy is effective to probe the local structure of materials because the Raman spectrum reflects the bonding states in the coordination polyhedra of a material. Raman spectra of Bi_2MoO_6 samples obtained at different pH value by hydrothermal method are shown in Fig. 7. All the typical vibrational bands for Bi_2MoO_6 samples are observed: 845 cm^{-1} (s), 815 cm^{-1} (w, sh), 797 cm^{-1} (vs), 715 cm^{-1} (m), 402 cm^{-1} (m), 354 cm^{-1} (s), 328 cm^{-1} (w), 292 cm^{-1} (m, sh), 282 cm^{-1} (s), 262 cm^{-1} (w, sh), 233 cm^{-1} (w), 200 cm^{-1} (m), 139 cm^{-1} (m) (Fig. 7A). All the samples showed the similar Raman vibration modes in the range of 100–450 cm^{-1}, and no apparent change of Raman shifts can be found. However, an obvious change of the Raman band intensity occurred in this range varying with the increasing of pH values in reaction system. As is shown in Fig. 7B, the intensity of band at 354 cm^{-1} remains the same all the time, while the intensity of 282 cm^{-1} increases gradually and the relative ratio of intensity at 282 and 354 cm^{-1} varies from 0.6 to 1.4, reflecting the difference in deformation degree of MoO_6 octahedra in different samples. It is well known that the bands in the 180–500 cm^{-1} region originates from the bending modes of the MoO_6 octahedra coupled with stretching and bending modes of the bismuth-oxygen polyhedra. The modes near 326, 345 and 402 cm^{-1} are corresponded to the E_u symmetry bending modes. And the intense Raman modes near 292, and 282 cm^{-1} originate most likely from the E_g mode bending vibration [32]. The dependence of the relative intensities of the asymmetric and symmetric deformational vibrations (282 and 354 cm^{-1}) of the MoO_6 octahedron on the synthesis conditions is observed, demonstrating that MoO_6 octahedra with different space symmetries are formed and the variation or rearrangement of the crystal structure exist under the influence of reaction conditions (pH value). The band at 139 cm^{-1} is assigned to the lattice modes of Bi^{3+} atoms mainly in the direction perpendicular to the layers.

In general, The Raman modes mainly at 797 cm^{-1} (A_{1g} mode) with two shoulders (782, 812 cm^{-1}) and 845 cm^{-1} (A_{2u} mode) can be assigned to the symmetric and asymmetric stretching vibrations of the WO_6 octahedra that involve motions of the apical oxygen atoms which are perpendicular to the layers [33]. The differences in the stretching vibrational bands provide interesting information on the structural variations. Variations in the width and the relative intensity of these two bands suggested that the stretching modes of the Mo—O bond are different (Fig. 7C). As the pH value increased, the strong band at 797 cm^{-1} was found to be shifted to 792 cm^{-1} and broadened. And the two shoulders at 782 and 812 cm^{-1} became prominent from pH 9 to pH 13. The shifts

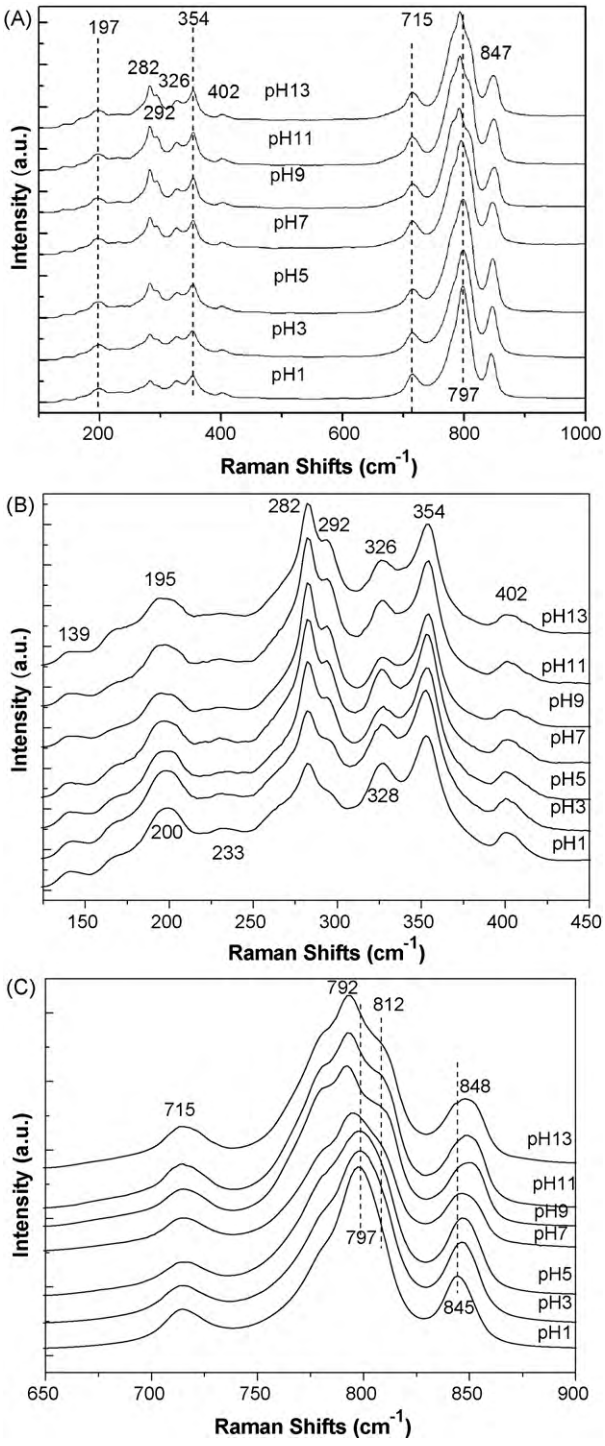

Fig. 7. Raman spectrum of Bi_2MoO_6 samples obtained at different pH value.

observed for Bi_2MoO_6 (pH 7, pH 9, pH 11, pH 13) were especially pronounced. The medium-intensity band was also broadened and also shifted in the position from 845 to 848 cm^{-1}. The absence of significant spectral variation from the samples (pH 1–7) revealed that the skeleton structure of the Bi_2MoO_6 phase was not dramatically disturbed. A similar Raman-band shift of the V—O stretching vibration was also observed in the Raman spectrum of $BiVO_4$ [12]. However, the observation of minute changes, such as the appearance of the triplet nature of the dominant Mo—O stretching bands at around 797 cm^{-1}, shift in position and broadening of the remaining Raman bands, suggested that there might be some subtle rear-

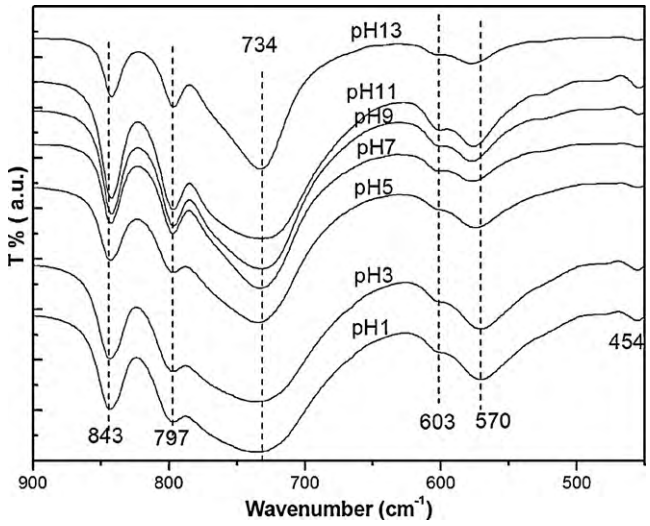

Fig. 8. FTIR of Bi_2MoO_6 samples obtained at different pH values.

rangements in the structure [34]. The obvious change of Raman modes for MoO_6 confirmed that the reaction condition (pH value) could result in the structure change of MoO_6 octahedra related to the apical oxygen atoms. However, the mode at 715 cm^{-1} exhibit no evident shift and broaden, which is due to the asymmetric stretching vibration (E_u mode) of the MoO_6 octahedra involving the motion of the equatorial oxygen atoms within layers, further confirming that the variation of MoO_6 structure only exist in the apical oxygen atoms not equatorial oxygen atoms.

The relationship between Raman stretching frequency and bond length was found to follow a simple exponential form:

$$R_{Mo-O} = 0.48239 \ln\left(\frac{32,895}{\nu}\right) \quad (1)$$

where ν is the Raman stretching frequency in wavenumbers and R is the metal–oxygen bond length in angstroms [35]. It can be concluded that the lower frequencies of the Raman stretching band correspond to the longer bond lengths. A calculation of the Mo—O bond length for Bi_2MoO_6 based on the expression suggests that one of the Mo—O (apical) bond length (797 cm^{-1}) increased from 1.793 Å in Bi_2MoO_6 (pH 1) to 1.798 Å Bi_2MoO_6 (pH 9). While the other apical Mo—O bond length (845 cm^{-1}) decreased from 1.767 Å in Bi_2MoO_6 (pH 1) to 1.764 Å in Bi_2MoO_6 (pH 13). The observation of the gradual increase and decrease in the bond lengths of the apical Mo—O distance strongly suggested the loose structure (weak symmetry constraint) existed in the samples synthesized at higher pH values. Several differences in half-widths and intensities of the diffraction peaks were observed in the XRD patterns of Bi_2MoO_6 synthesized hydrothermally at various pH values (Fig. 1), indicating that slight changes in the structure, even though all the powders exhibited the monoclinic koechilinite phase.

Fig. 8 shows the FTIR spectra of Bi_2MoO_6 samples obtained at different pH values. The main absorption bands at 400–900 cm^{-1} are mainly related to Bi—O, Mo—O stretching and Mo—O—Mo bridging stretching modes, which can reflects the variation of structure in crystal [33]. The bands at around 843 and 797 cm^{-1} can be assigned as the asymmetric and symmetric stretching mode of MoO_6 involving vibrations of the apical oxygen atoms, respectively. The band at 734 cm^{-1} is attributed to the asymmetric stretching mode of MoO_6 involving vibrations of the equatorial oxygen atoms and the bands at 603, 570 cm^{-1} correspond to the bending vibration of MoO_6. As seen from the figure, the bands of MoO_6 at 797 and 603 cm^{-1} for all the samples are similar and no shifts can be found. Minor downshifts of wavenumber at 843 cm^{-1} and great upshifts at 570 cm^{-1} are observed, indicating that the variation of structure for MoO_6 octahedra may be occurred with the increasing of pH values in this system. Furthermore, a small change of the band occurred at 454 cm^{-1}, which is attributed to the stretching and bending vibrations of BiO_6 octahedra, further confirming the changes of crystal structure. Based on the above results and analysis, it can be concluded that the changing of pH value in reaction system may influence the crystal structure and corresponding photocatalytic performance.

In orthohombic Bi_2MoO_6, the molybdenum cation is located in a distorted MoO_6^{2-} octahedron with different distinct bond lengths, and the bismuth cation is coordinated with the MoO_6^{2-} octahedrons. Consequently, the lone-pair distortion existed in the orthohombic structure due to the difference in the Bi—O bond lengths around the bismuth cation. Based on the above discussion, it can be concluded that the lone-pair distortions around the bismuth cation in Bi_2MoO_6 prepared at higher pH values (pH 9, pH 11, pH 13) are less than those of Bi_2MoO_6 (pH 1, pH 3, pH 5). Therefore, the delocalization of photogenerated electron and hole pairs for Bi_2MoO_6 prepared at the higher pH values is less than that at low pH value. The distortion degree of the MoO_6 octahedron in the local structure of Bi_2MoO_6 could result in a distinct variation in the electronic structure [12]. The greater the degree of distortion of the local structure, the more the Bi 6s and O 2p orbitals overlap, which enhances the migration of photogenerated holes [12]. It is reasonable that the Bi_2MoO_6 samples obtained under basic conditions showed the lower photocatalytic activities. The order of the photocatalytic activities for the hydrothermally synthesized Bi_2MoO_6 samples agrees well with the degree of lone-pair distortion indicated by Raman shifts. The degree of distortion of Bi_2MoO_6 (pH 3) was similar to that of Bi_2MoO_6 (pH 5), and thus their photocatalytic activities are comparable. The photocatalytic activity of Bi_2MoO_6 (pH 1) was lower than that of Bi_2MoO_6 (pH 3, pH 5) can be attributed to the relatively small BET surface area (6.38 m^2/g).

4. Conclusions

The transformation of the Bi_2MoO_6 morphology from a 2D sheet-like structure to a 1D rod-like has been realized through a facile, pH-controlled, surfactant-free hydrothermal route. The Bi_2MoO_6 sample prepared at acidic condition exhibited a photocatalytic activity 12 times higher than that prepared at basic condition for the photodegradation of MB under visible-light irradiation. The relationship between the initial pH value, morphology, variation of local structure, and photocatalytic activity of Bi_2MoO_6 was elucidated. Our work suggests that the photocatalytic performance of Bi_2MoO_6 is greatly dependent on the local structure and the morphology. The hydrothermal technique presented here seems an economical and easy way for the morphology and local structure control of such material.

Acknowledgements

This work was partly supported by the National Natural Science Foundation of China (20925725 and 50972070) and National Basic Research Program of China (2007CB613303).

References

[1] M.R. Hoffmann, S.T. Martin, W.Y. Choi, D.W. Bahnemann, Chem. Rev. 95 (1995) 69–96.
[2] N. Baux, R.N. Vannier, G. Mairesse, G. Nowogrocki, Solid State Ionics 91 (1996) 243.
[3] M.S. Islam, S. Lazure, R.N. Vannier, G. Nowogrocki, G.J. Mairesse, Mater. Chem. 8 (1998) 655.
[4] O.M. Bordun, Inorg. Mater. 34 (1998) 1270.
[5] A. Kudo, S. Hijii, Chem. Lett. 10 (1999) 1103.
[6] J.W. Tang, Z.G. Zou, J.H. Ye, Catal. Lett. 92 (2004) 53.

[7] H. Fu, C. Pan, W. Yao, Y. Zhu, J. Phys. Chem. B 109 (2005) 22432.
[8] J.G. Yu, J.F. Xiong, B. Cheng, Y. Yu, J.B. Wang, J. Solid State Chem. 178 (2005) 1968.
[9] J.H. Bi, L. Wu, J. Li, Z.H. Li, X.X. Wang, X.Z. Fu, Acta Mater. 55 (2007) 4699.
[10] L.S. Zhang, W.Z. Wang, L. Zhou, H.L. Xu, Small 3 (2007) 1618.
[11] L. Lu, A. Kobayashi, K. Tawa, Y. Ozaki, Chem. Mater. 18 (2006) 4894.
[12] J.Q. Yu, A. Kudo, Adv. Funct. Mater. 16 (2006) 2163–2169.
[13] L.S. Zhang, J.L. Li, Z.G. Chen, Y.W. Tang, Y. Yu, Appl. Catal. A 299 (2006) 292.
[14] J.F. Wang, M.S. Gudiksen, X.F. Duan, Y. Cui, C.M. Lieber, Science 293 (2001) 1455.
[15] J. Hu, L. Li, W. Yang, L. Manna, L. Wang, A.P. Alivisatos, Science 292 (2001) 2060.
[16] L.W. Zhang, Y.J. Wang, H.Y. Cheng, W.Q. Yao, Y.F. Zhu, Adv. Mater. 21 (2009) 1286.
[17] H.L. Xu, W.Z. Wang, W. Zhu, J. Phys. Chem. B 110 (2006) 13829.
[18] S.H. Yu, L. Biao, M.S. Mo, J.H. Huang, X.M. Liu, Y.T. Qian, Adv. Funct. Mater. 13 (2003) 639.
[19] Y.W. Jun, J.S. Choi, J. Cheon, Angew. Chem. Int. Ed. 45 (2006) 3414.
[20] N. Kim, R.N. Vannier, C.P. Grey, Chem. Mater. 17 (2005) 1952–1958.
[21] C.J. Murphy, Science 298 (2002) 2139.
[22] A.B. Panda, G. Glaspell, M.S. El-Shall, J. Phys. Chem. C 111 (2007) 1861–1864.
[23] V.F. Puntes, D. Zanchet, C.K. Erdonmez, A.P. Alivisatos, J. Am. Chem. Soc. 124 (2002) 12874.
[24] J. Park, K. An, Y. Hwang, J.-G. Park, H.-J. Noh, J.-Y. Kim, J.-H. Park, N.-M. Hwang, T. Hyeon, Nat. Mater. 3 (2004) 891.
[25] H.W. Liao, Y.F. Wang, X.M. Liu, Y.D. Li, Y.T. Qian, Chem. Mater. 12 (2000) 2819.
[26] W. Fan, Y. Bu, X. Song, S. Sun, X. Zhao, Cryst. Growth Des. 11 (2007) 2361.
[27] H.L. Wang, X.D. Ma, X.F. Qian, J. Yin, Z.K. Zhu, J. Solid State Chem. 177 (2004) 4588.
[28] Y. Shimodaira, H. Kato, H. Kobayashi, A. Kudo, J. Phys. Chem. B 110 (2006) 7790.
[29] A. Hagfeldt, M. Gratzel, Chem. Rev. 95 (1995) 49.
[30] C. Zhang, Y. Zhu, Chem. Mater. 17 (2005) 3537.
[31] T. Zhang, T. Oyama, A. Aoshima, H. Hidaka, J. Zhao, N. Serpone, J. Photochem. Photobiol. A: Chem. 140 (2001) 163.
[32] M. Maczka, J. Hanuza, W. Paraguassu, A.G. Souza Filho, P.T. Freire, C.J. Mendes Filho, Appl. Phys. Lett. 92 (2008) 112911.
[33] M. Maczka, W. Paraguassu, A.G. Souza Filho, P.T.C. Freire, J. Mendes Filho, J. Hanuza, Phys. Rev. B 77 (2008) 094137.
[34] R. Murugan, Physica B 352 (2004) 227.
[35] Franklin D. Hardcastle, Israel E. Wachs, J. Phys. Chem. 95 (1991) 10763.